Bio-Design and Manufacturing (2025) 8:423–441
https://doi.org/10.1631/bdm.2400108

RESEARCH ARTICLE

Bioprinted integrated gradient biomechanical signal-tailored osteosarcoma model: advancing insights into tumor development and drug screening

Xuelian Mi[1] · Ya Ren[1,2] · Hanbo Wang[3] · Lei Qiang[4] · Weiqing Kong[5] · Hui Wang[6] · Xue Yang[2] · Yihao Liu[7,8] · Han Yang[7,8] · Di Xiao[9] · Zhenjiang Ma[7,8] · Guoxing Xu[10] · Changru Zhang[7,8] · Jinwu Wang[1,7,8]

Received: 21 March 2024 / Accepted: 15 September 2024

Abstract

In the current settings of osteosarcoma research and drug screening, in vitro three-dimensional (3D) models, which overcome the limitations of traditional models, are favored. In in vitro 3D models, tumor microenvironment simulation, particularly of the mechanical microenvironment, is crucial for estimating the biological effects of a tumor. However, current in vitro osteosarcoma model construction is often limited to a single mechanical signal, which fails to simulate the diversity of osteosarcoma mechanical stimuli. In this study, we utilized embedded bioprinting technology and the multiple response properties of calcium ions in soft and hard stiffness systems with osteosarcoma cell biological functions to construct an integrated gradient biomechanical signal-tailored osteosarcoma model (IGBSTOM). We achieved this by printing a fibrinogen bioink containing calcium ions and osteosarcoma tumor spheroids within an extracellular matrix composed of methacryloylated alginate, methacryloylated gelatin, thrombin, and transglutaminase, which is rich in polysaccharides and proteins and exhibits self-healing properties. Our in vitro and in vivo studies showed that the IGBSTOM enhanced tumor stemness, proliferation, and migration, and successfully reproduced the nest-like structure of tumors, providing an in vitro research platform that is more similar to the natural tumor than the existing models. This study proposes a novel IGBSTOM construction and provides a new strategy for the clinical understanding of tumor development, drug screening, and exploration of drug resistance and metastasis mechanisms.

Xuelian Mi, Ya Ren, and Hanbo Wang have contributed equally to this work.

✉ Changru Zhang
zcr_ecust@163.com

✉ Jinwu Wang
wangjw-team@shsmu.edu.cn

[1] Institute of Biomedical Engineering, College of Medicine, Southwest Jiaotong University, Chengdu 610031, China

[2] State Key Laboratory of Biotherapy and Cancer Center, West China Hospital, Sichuan University, Chengdu 610041, China

[3] Orthopaedic Bioengineering Research Group, Division of Surgery and Interventional Science, University College London, London HA7 4LP, UK

[4] Key Laboratory of Advanced Technologies of Materials (Ministry of Education), School of Materials Science and Engineering, College of Medicine, Southwest Jiaotong University, Chengdu 610031, China

[5] Department of Spinal Surgery, The Affiliated Hospital of Qingdao University, Qingdao 266000, China

[6] Engineering Research Center for TCM Intelligent Rehabilitation (Ministry of Education), School of Rehabilitation Science, Shanghai University of Traditional Chinese Medicine, Shanghai 201203, China

[7] Shanghai Key Laboratory of Orthopaedic Implants, Department of Orthopaedics, Ninth People's Hospital Affiliated to Shanghai Jiao Tong University School of Medicine, Shanghai 200011, China

[8] School of Biomedical Engineering, Shanghai Jiao Tong University, Shanghai 200030, China

[9] Liuzhou Traditional Chinese Medical Hospital, Guangxi University of Chinese Medicine, Liuzhou 545001, China

[10] Department of Orthopedics, Jiading District Anting Hospital of Shanghai, Shanghai 201805, China

Graphical abstract

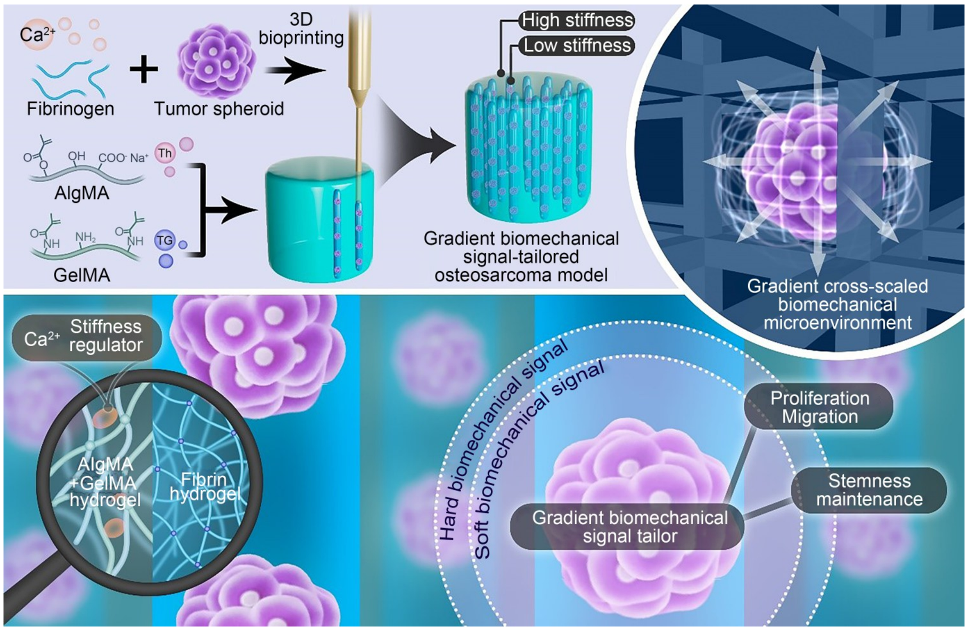

Keywords 3D bioprinting · Gradient biomechanical signal-tailored model · Osteosarcoma · Tumor development · Drug screening

1 Introduction

Osteosarcoma, the most common type of malignant bone tumor, is characterized by high aggressiveness and heterogeneity and poses great challenges for patient survival and treatment [1, 2]. In vitro tumor models have become important tools for studying malignant tumors due to their advantages, which include high-throughput drug screening, avoidance of animal ethical issues, cost-effectiveness, and their applications in mechanistic studies and personalized medicine. Over the past few decades, developments such as simple two-dimensional (2D) monolayer tumor cell culture and xenograft animal tumor models have provided important insights into osteosarcoma and led to the development of new therapies. However, 2D monolayer tumor cell culture models lose tumor-specific morphology, function, and metabolic activity and lack cell–cell and cell–extracellular matrix (ECM) interactions. In addition, the biology of tumor cells is altered in 2D culture systems, leading to experimental limitations and a high failure rate for drug treatment regimens. The application of animal tumor models has limitations such as long modeling time, high costs, and animal ethical issues [3, 4].

In recent years, in vitro three-dimensional (3D) tumor models have received widespread attention due to their likeness to the 3D structure of in vivo tumor tissues and their effective simulation of the tumor microenvironment. The construction of the tumor mechanical microenvironment in in vitro tumor models, particularly ECM stiffness in the tumor mechanical microenvironment, affects tumor proliferation, angiogenesis, metabolism, invasion, migration, and metastasis [5, 6]. During tumor development, tumor cells remodel the surrounding ECM, and ECM around the tumor forms a gradient structure with a soft inner layer and a hard outer layer [7, 8]. Although biomechanical characterization for osteosarcoma is limited at present, we can gain some insights from studies on other types of tumors. Xu et al. [9] reported that the Young’s modulus of ovarian cancer cells is approximately 0.8 kPa, measured by atomic force microscopy (AFM). Similarly, a study by Plodinec et al. [10] revealed that the Young’s modulus of breast cancer cells is approximately 0.75 kPa. Simultaneously, mechanical signals from ECM regulate the biological functions of tumor cells. Macroscopically, osteosarcoma typically occurs in the proximal metaphysis of long bones [11], a region that contains much collagenous bone tissue. During growth, osteosarcoma tissues directly contact the surrounding collagenous bone tissues to form a macroscopically hard biomechanical microenvironment, which gradually undergoes protein secretion and deposition during development, forming a microcosmically soft biomechanical microenvironment inside the solid tumor [12]. Therefore, it is of great significance to construct an in vitro tumor model with tailored gradient biomechanical signals to simulate the gradient biomechanical signal characteristics of natural solid tumors and to reproduce the biological phenotypes of natural tumor tissues in order to study the mechanisms of tumorigenesis, drug screening, treatment, drug resistance, and metastasis in osteosarcoma. Numerous researchers have constructed in vitro 3D models of osteosarcoma to perform a series of studies. However, no study has replicated an in vitro osteosarcoma model constructed with gradient biomechanical signals to mimic the gradient biomechanical signal characteristics of natural solid tumors [13–16].

Gelatin, derived from type I collagen, is a core ECM component in tumor and bone microenvironments. Upon reaction with methacrylic anhydride, gelatin can be converted into photocrosslinkable gelatin methacrylate (GelMA), which has been widely used to mimic natural ECM in in vitro disease models [17, 18]. Alginate, a polysaccharide extracted from natural seaweed, possesses excellent biocompatibility but relatively weak mechanical properties. However, when reacting with methacrylic anhydride, alginate is transformed into methacrylated alginate (AlgMA), which retains its excellent biocompatibility and superior mechanical properties. When GelMA and AlgMA undergo crosslinking under ultraviolet (UV) irradiation, they form hydrophilic biopolymer hydrogels with 3D network structures. In addition, calcium ions form physical crosslinks with the carboxyl groups in AlgMA via electrostatic interactions, forming egg-box-like structures and thus remarkably enhancing the structural integrity of the hydrogel [19–21]. In recent years, enzymatically crosslinked fibrin hydrogels based on fibrinogen, thrombin (Th), and transglutaminase (TG) have gained widespread attention due to their ability to form stable 3D structures, thereby providing suitable microenvironments for in vitro tumor models [22, 23]. Notably, calcium ions play a pivotal role in our unique model system, demonstrating distinctive effects within soft and hard stiffness systems and exhibiting multifaceted response characteristics in regulation of the biological functions of osteosarcoma cells. First, in the high-stiffness AlgMA system, calcium ions play a pivotal role in enhancing the system stability by facilitating physical crosslinking with AlgMA, forming a reversible network structure. Second, in the low-stiffness fibrin system, calcium ions activate TG, which promotes the covalent crosslinking of fibrin peptides following Th cleavage, forming stable fibrin hydrogels. In addition, calcium ions participate in and regulate key biological behaviors, such as proliferation, migration, and invasion of osteosarcoma cells.

Bioprinting technology, an emerging 3D tissue engineering method, is a powerful tool for constructing simulation models. By precisely controlling the arrangement of biomaterials and the distribution of cells, bioprinting technology can simulate the complex structure of in vivo tissues. Particularly in the field of tumor research, the application of bioprinting technology has provided groundbreaking opportunities, enabling the construction of more realistic and controllable tumor models [24, 25]. However, it is difficult to achieve high cell densities similar to those of natural tissues by co-mixing conventional bioinks with cells [26]. To address this challenge, in this study, we used precultured tumor spheroids to achieve high cell density, pH, oxygen, nutrient and metabolic gradients, and necrotic region properties to mimic natural human solid tumors [27].

In this study, we proposed a fast and convenient design strategy to simulate the gradient biomechanical signal characteristics of osteosarcoma. A soft ECM adapted to the modulus of osteosarcoma cells was constructed to simulate a microscopic soft biomechanical microenvironment, whereas a hard biomechanical microenvironment adapted to the modulus of collagenous bone tissue was constructed to simulate the macroscopic conditions. We achieved this by printing a fibrinogen bioink containing calcium ions and osteosarcoma tumor spheroids within ECM composed of AlgMA, GelMA, Th, and TG, which is rich in polysaccharides and proteins and exhibits self-healing properties (Fig. 1). This innovative model simulated the gradient biomechanical signal characteristics of osteosarcoma and provided an in vitro research platform that closely mimics natural tumors.

2 Materials and methods

2.1 Materials and reagents

Fibrinogen and Th were acquired from Yeasen Biotechnology (Shanghai, China). GelMA, AlgMA, and phenyl-2,4,6-trimethylbenzoylphosphinate (LAP) were obtained from EFL at Suzhou Intelligent Manufacturing Research Institute, China. TG was acquired from Sigma-Aldrich (St. Louis, MO, USA). Lumbrokinase, doxorubicin, and methotrexate were acquired from Aladdin Reagent Co. (Shanghai, China). Rhodamine B and calcium chloride ($CaCl_2$) were acquired from Macklin (Shanghai, China). MG-63 (human osteosarcoma cell line) was obtained from Fu Heng Biology (Shanghai, China). Antibiotics (penicillin/streptomycin) and Dulbecco's modified Eagle medium (DMEM) were acquired from Gibco BRL (Shanghai, China). Fetal bovine serum was acquired from Sigma-Aldrich. For the in vivo experiments, male BALB/c nude mice from Shanghai Jihui Laboratory Animal Care Co., Ltd. were used.

2.2 Osteosarcoma spheroid culture

MG-63 cells were maintained at 37 °C under 5% CO_2, in accordance with the manufacturer's guidelines. MG-63

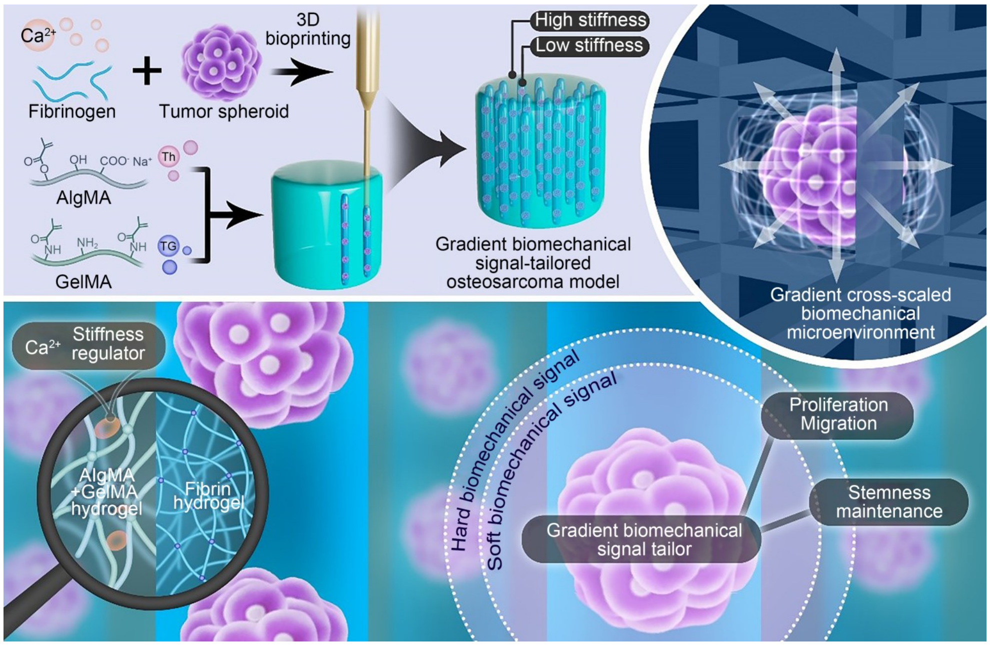

Fig. 1 Schematic representation of the 3D bioprinting method for the integrated gradient biomechanical signal-tailored osteosarcoma model. Fibrinogen containing osteosarcoma tumor spheroids and calcium ions was used as the bioink for printing in an AlgMA/GelMA bioink bath supplemented with Th and TG. Th and TG interacted with the fibrinogen and polymerized during the printing process, forming a soft fibrin hydrogel inside the hard AlgMA/GelMA hydrogel. This method creates an integrated gradient biomechanical signal-tailored osteosarcoma model. In the experimental design, this model is referred to as the Ca^{2+}-G/OS group

cells were cultured until 80% confluence was reached and routinely passaged using trypsin. The cell culture medium was changed every 2 d. Upon reaching approximately 80% confluence, the cells were detached from the culture dishes using trypsin and subsequently suspended in the cell culture medium. According to the manufacturer's requirements, 3D tumor spheroids comprising MG-63 cells were fabricated using ultra-low adhesion 96-well U-bottom microplates (EFL, Suzhou, China). To achieve ideal cellular density for producing dense 3D in vitro models, MG-63 cell suspensions with different cellular densities (1×10^5, 2×10^5, and 3×10^5 cells/mL, denoted as SD-1, SD-2, and SD-3, respectively) were prepared. A volume of 100 µL of each cell suspension was added to each well of 96-well U-bottom microplates. Cellular aggregation, size, and 3D spheroid morphological features were monitored periodically using an inverted fluorescence microscope (Olympus CKX53, Japan). Tumor spheroids were cultured in an incubator at 37 °C under 5% CO_2 and were monitored every 12 h.

2.3 Bioink preparation and bioprinting

GelMA (10% (100 mg/mL)) and LAP (0.5% (5 mg/mL)) were dissolved in deionized water at 55 °C, and different concentrations of AlgMA were added to the solution. The following AlgMA/GelMA mixtures were prepared: 1% AlgMA with 10% GelMA (1A10G), 2% AlgMA with 10% GelMA (2A10G), and 4% AlgMA with 10% GelMA (4A10G). The hydrogel solution was filtered through a 0.22-µm filter (Millipore, MA, USA) to remove bacteria. The hydrogel solution was carefully poured into a cylindrical mold and crosslinked under a UV lamp at a wavelength of 365 nm for 60 s. Once the crosslinking of covalent AlgMA/GelMA was observed, the hydrogel was removed from the mold and soaked in 1.8 mmol/L $CaCl_2$ for 2 h to allow for the ion crosslinking of AlgMA.

The fibrinogen solution (10 mg/mL) was produced by dissolving lyophilized bovine plasma protein at 37 °C in sterile physiological saline with 1.8 mmol/L $CaCl_2$ for 1 h. The solution was filtered through a 0.22-µm filter and stored at 4 °C. To prepare a stock solution of Th, lyophilized Th was reconstituted at 100 U/mL using physiological saline stored at −20 °C. Crosslinking was performed using physiological saline diluted to 10 U/mL of Th and 3% (30 mg/mL) TG working solution. The mixed solution of Th and TG was passed through a 0.22-µm filter and then stored at 4 °C.

The tumor model was fabricated using a 3D bioprinter (Biobulid-S, China). Before printing, the bioprinter was sterilized with UV light on an ultra-clean table. Next, 500 precultured osteosarcoma tumor spheroids were mixed with 10 mg/mL fibrinogen solution and pre-crosslinked with 1 U/mL Th. The temperature of the nozzle was set at 20 °C, and the printed structures were immersed in an AlgMA/GelMA bioink bath containing 0.5% photoinitiator. Printing was performed using a 16G needle at an extrusion speed of 15 µL/min. The printed structures underwent UV crosslinking for 60 s, followed by culture in a DMEM conditioned medium containing 1.8 mmol/L calcium ions.

2.4 Rheological and mechanical characterization

The rheological properties of the prepolymers and hydrogels were assessed using a rheometer (Discovery HR20, TA, USA). A 20.0-mm parallel plate (Peltier plate, stainless steel) was used for all measurements. To evaluate shear-thinning, measurements were implemented with the shear rate increased from 0 to 100 s^{-1} at 25 °C. A frequency sweep assay was conducted on the mixtures across a frequency range of 0.1–100 Hz while maintaining a constant temperature of 25 °C. During this process, both the storage modulus (G') and loss modulus (G'') were recorded.

Compression testing of the AlgMA/GelMA hydrogel was performed using a universal testing machine (AG-2000A, Japan). Prior to testing, the AlgMA/GelMA hydrogel was formed into a cylinder with a diameter of 5 mm. The compression modulus of a hydrogel, defined as stress/strain, corresponds to the gradient of the initial linear segment observed on the stress–strain curves. In this study, the strain of the hydrogel was 10%–15%, representing a linear region that reflects the behavior of the hydrogel in the elastic phase. We performed linear fitting to calculate the compression modulus of the hydrogel.

2.5 AFM

Fibrin hydrogels based on the principle of human blood clotting are often characterized by weak mechanical properties. AFM is a non-destructive test method and can measure the mechanical properties of sample surfaces at the nanoscale, which can be used to characterize the elastic modulus of cellular materials and materials with weak mechanical properties. In this method, the AFM probe touches the sample surface, applies small forces, and measures the response of the sample to these forces to determine its elastic modulus. The mechanical properties of osteosarcoma cells and fibrin hydrogels were assessed using Bruker's AFM method in the force−curve scanning mode. This mode enables the measurement of the force–displacement relationship at various locations in the sample, allowing for the calculation of the sample's elastic modulus. The resulting curve was fitted using the Hertz–Sneddon model to extrapolate the apparent Young's modulus. Data analysis was conducted using Nanoscope Analysis software.

2.6 Scanning electron microscopy (SEM) and energy dispersive spectroscopy (EDS)

SEM was used to characterize the porosity of the hydrogels with different concentration ratios. A tailored osteosarcoma model with an integrated gradient biomechanical signal into the bioprinted constructs was observed using SEM (Tescan, Czech Republic). In brief, samples were fixed in glutaraldehyde at 25 °C for 1 h and then freeze-dried. The elemental distributions of the constructs were investigated via EDS (Tescan).

2.7 Cell counting kit-8 (CCK-8) assay

The effect of calcium ions on the proliferation of 2D osteosarcoma cells was monitored as follows. On Day 0, MG-63 cells were plated into 96-well plates at a density of 2000 cells/well. Osteosarcoma cells were cultured in a conditioned medium with 0, 0.9, 1.8, 2.7, 3.6, or 4.5 mmol/L of calcium ions. On Days 1, 3, and 5, cells were incubated with 100 μL of the conditioned medium containing 10% CCK-8 reagent (Beyotime, China) at 37 °C for 2 h. Absorbance of light at 450 nm was detected using a microplate reader (Synergy Neo2, BioTek, USA).

The effect of calcium ions on the proliferation of osteosarcoma spheroids was monitored as follows. Osteosarcoma cells were seeded into a 96-well U-bottom cell culture plate at a density of 2000 cells/well and incubated at 37 °C for 24 h. Subsequently, the medium was aspirated, and each well was replenished with the conditioned medium either containing calcium ions at a concentration of 1.8 mmol/L or not. Absorbance at 450 nm was detected on Days 1, 3, and 5 following the aforementioned protocol.

2.8 Fibrin hydrogel degradation test

Three groups of fibrin hydrogels were prepared using the molding method: (1) fibrinogen and Th crosslinking, (2) fibrinogen crosslinking with Th and TG, and (3) fibrinogen crosslinking with Th and TG containing calcium ions. The initial mass of the fibrin hydrogel was recorded as W_0. Subsequently, 10 U/mL of lumbrokinase was added, and the hydrogel was incubated at 37 °C for 2 h, after which the weight was measured as W_1. The degradation rate of the fibrin hydrogel was calculated using the formula $(W_0-W_1)/W_0\times100\%$.

2.9 Live/Dead assay

The viability of the osteosarcoma model was evaluated using a live/dead cell staining kit (Yeasen, China) on Days 1 and 7, in accordance with the manufacturer's instructions. After removing the culture medium from the tumor model, the model underwent two washes with phosphate-buffered saline (PBS). Subsequently, the model was incubated in a solution containing 2 μmol/L calcein acetoxymethyl and 4.5 μmol/L propidium iodide for 30 min at 37 °C in the dark. Following the removal of the dye solution under subdued lighting, the cells were rinsed twice with PBS. The samples were then examined using a laser-scanning confocal microscope (LSCM; Leica, Germany).

2.10 5-ethynyl-2′-deoxyuridine (EdU) proliferation experiment

The osteosarcoma model was first cultured in DMEM high-glucose medium for 24 h. Then, the medium was removed, and the cells were washed with PBS. Subsequently, the cells were labeled using a 1 : 1000 dilution of EdU solution and incubated for 4 h at 37 °C in an incubator. After labeling, the cells were fixed with 4% paraformaldehyde, and excess fixative was removed by washing with PBS. Next, the cells were permeabilized using 0.5% Triton X-100 solution and washed again with PBS. Following permeabilization, the cells were stained with Apollo staining solution (RiboBio, Guangzhou, China) and incubated for 30 min in the dark. After removing the excess staining solution by washing with PBS, the cell nuclei were stained with 4′,6-diamidino-2-phenylindole (DAPI) staining solution at a 1 : 1000 dilution and incubated for 10 min at 25 °C in the dark. Finally, the cells were washed with PBS and then observed and photographed using a confocal microscope.

2.11 RNA extraction and reverse transcription quantitative polymerase chain reaction (RT-qPCR)

Prior to the experiments, to further validate the biological effects of calcium ions in model construction and the effects of gradient biomechanical signaling in the customized osteosarcoma model, we divided the experiments into the following four groups: OS, Ca^{2+}-OS, Ca^{2+}-S/OS, and Ca^{2+}-G/OS. The OS group consisted of osteosarcoma spheroids without calcium ions; the Ca^{2+}-OS group included osteosarcoma spheroids with added calcium ions; the Ca^{2+}-S/OS group represented osteosarcoma spheroids embedded in a soft fibrin hydrogel containing calcium ions; and the Ca^{2+}-G/OS group featured a 3D tumor model with a soft fibrin interior and a hard AlgMA/GelMA hydrogel exterior, constructed with calcium ions using 3D bioprinting. OS and Ca^{2+}-OS samples were collected in a 15-mL centrifuge tube, centrifuged at 1000 r/min for 5 min at 25 °C, and then suspended in TRIzol reagent (Sangon Biotech, China). Ca^{2+}-S/OS and bioprinted Ca^{2+}-G/OS tumors were washed three times with PBS (1 min each time), transferred to a 6-well plate containing an ophthalmic shear hydrogel, and then added with TRIzol reagent.

For genetic analysis, total RNA was isolated from the cells using TRIzol reagent. Reverse transcription was conducted to convert the extracted mRNA into cDNA utilizing a Prime Script RT kit (Yeasen, China) in conjunction with a SYBR Green RT-qPCR kit (Yeasen). This was followed by real-time PCR analysis using equipment from Thermo Fisher Scientific (USA). The procedures were performed in accordance with the manufacturer's guidelines, and the primer sequences for each gene are shown in Table S1 (supplementary information).

2.12 Immunofluorescence

Four tumor models—OS, Ca^{2+}-OS, Ca^{2+}-S/OS, and Ca^{2+}-G/OS—were established over a period of 4 d. Samples from each group were fixed with 4% paraformaldehyde for 20 min and subsequently washed three times with PBS. Following a 15-min incubation with 0.5% Triton X-100 in PBS, the samples were blocked in PBS containing 5% bovine serum albumin (BSA; BioFroxx, Germany) for 1 h. Primary anti-cluster of differentiation 133 (CD133) (1 : 400; Proteintech, China), anti-vimentin (1 : 400; Proteintech), and anti-SRY-box transcription factor 2 (SOX2) (1 : 400; Proteintech) were applied overnight at 4 °C. Subsequently, secondary antibodies were incubated with the samples for 2 h at room temperature. Finally, nuclei were stained with DAPI for 15 min. Observation was conducted using LSCM.

2.13 Establishment and evaluation of the in vivo tumor mouse model

Before the experiment, BALB/c nude mice were weighed individually to calculate the appropriate amount of anesthetic to be administered. During the anesthesia procedure, the heads were tilted back slightly to move the lower abdominal organs upward. The injection site was sterilized using iodophor-soaked cotton balls. A 1% sodium pentobarbital solution, at a dose of 50 mg/kg, was injected into the lower abdomen of the mice, 0.5 cm on either side of the midline (at the root of the thigh). The depth of anesthesia was confirmed by stimulating the toe response, after which the subsequent experiments were performed. Once disinfection was completed, the skin was incised and the four groups of osteosarcoma models which had been precultured for 4 d were implanted. After implantation, the tumors were closed using absorbable surgical sutures, and povidone–iodine was applied to the wound sutures. The nude mice were then placed into cages and monitored for vital signs. Two weeks after tumor implantation, the nude mice were euthanized via cervical dislocation, and the tumor tissues were removed and transferred to 4% paraformaldehyde for subsequent histological evaluation.

2.14 Histological evaluations and immunofluorescence

The nude mice were euthanized 14 d after the tumor models were transplanted. The tumor tissues were removed and fixed with 4% paraformaldehyde. Sections (5 μm) were stained with hematoxylin and eosin (H&E) and with immunofluorescent dyes to visualize cellular structures and markers. They were fluorescently double-stained with CD133 and proliferation marker protein Ki-67 (Ki67) to express tumor stem and proliferation markers respectively and then scanned. Furthermore, the sections were fluorescently double-stained with platelet endothelial cell adhesion molecule (CD31) and alpha-smooth muscle actin (α-SMA) to examine the formation of tumor vessels and stained with SOX2 to express tumor stem markers. For immunofluorescence, these sections were permeabilized with 0.3% Triton X-100 for 15 min and then incubated with 5% BSA for 1 h at room temperature to block nonspecific binding. These sections were incubated with anti-CD133 (1 : 400), anti-SOX2 (1 : 400), anti-Ki67 (1 : 400), anti-CD31 (1 : 400), and anti-α-SMA (1 : 400) overnight at 4 °C, and then incubated with secondary antibodies for 2 h at room temperature. Finally, DAPI was applied for 15 min to stain the cell nuclei.

2.15 Drug permeability test and chemotherapeutic drug efficacy

After washing with PBS, 3D models were briefly exposed to rhodamine B (10 μg/mL) for 3 h at 37 °C, followed by observation and imaging using an LSCM. Subsequently, tumor models were treated with varying concentrations (0, 0.1, 1, 10, 100, or 500 μmol/L) of doxorubicin and methotrexate for 48 h. Cell viability was assessed via the CCK-8 assay.

2.16 RNA-seq analysis

Libraries were assembled in accordance with the guidelines provided by the manufacturer (BGI-Shenzhen, China). Bioinformatics analysis of RNA sequencing data was conducted using Dr. Tom by BGI Genomics. A heatmap was generated based on the expression levels of the gene transcripts in different samples. Following the adjustment for significant pathway levels, Kyoto Encyclopedia of Genes and Genomes (KEGG) enrichment and gene set enrichment analysis (GSEA) were conducted on the differentially expressed genes (DEGs).

2.17 Statistical analysis

Data were recorded as mean±standard deviation. Group differences were assessed using Tukey's post-hoc test and one-way analysis of variance (ANOVA). Statistical analyses were conducted using GraphPad Prism software. Statistical significance was defined as $^{*}P<0.05$, $^{**}P<0.01$, and $^{***}P<0.001$.

3 Results and discussion

3.1 Design, preparation, and characterization of the bioink

The design and selection of bioinks are crucial steps in bioprinting because they affect the mechanical properties of tissues as well as cell behavior and function. Gelatin, derived from type I collagen, is a biocompatible biomaterial and a major component of tumor ECM and bone microenvironment [28]. When reacting with methacrylic anhydride, gelatin is transformed into GelMA to produce photocrosslinkable hydrogels that are widely used to mimic ECM in in vitro disease models [29]. Sodium alginate is commonly used in bioinks because of its excellent biocompatibility. However, its poor mechanical properties limit its applications. As both the –OH and –COOH groups in its structural units can serve as reactive sites, sodium alginate can react with methacrylic anhydride to form AlgMA, which has good biocompatibility and excellent mechanical properties. GelMA and AlgMA can undergo crosslinking reactions under UV light exposure, forming elastic, hydrophilic polymer networks with 3D structures. In addition, calcium ions form physical crosslinks with the carboxyl groups in AlgMA through electrostatic attraction, resulting in the formation of a physically crosslinked egg-box-like structure [30]. The crosslinked methacrylate (MA) groups contribute to the structural integrity of the hybrid hydrogel while the physically crosslinked calcium ions form a reversible network. Under stress, the UV light and calcium ion-mediated dual-crosslinked interpenetrating network hydrogel dissipates energy, enhancing its mechanical properties (Fig. 2a).

To optimize the interpenetrating network hydrogel and match the macroscopic collagenous bone tissue biomechanical signals, we investigated the performance of various concentrations of AlgMA (1%, 2%, and 4%) while maintaining the GelMA concentration at 10%. According to previous reports, 10% GelMA maintains cell viability, stimulates proliferation, and produces stable cultured gels, demonstrating a relatively high proliferative capacity [31]. Rheological analysis of the three hydrogels showed that as the angular frequency varied from 1 to 100 rad/s, the interpenetrating polymer networks remained predominantly elastic, with no observed changes in G', indicating that the interpenetrating network hydrogel had stable elastic properties (Fig. 2b). The hybrid hydrogels of UV-crosslinked AlgMA and GelMA exhibited higher G' than G'', demonstrating the replication of the complex 3D microenvironment required for tumor growth.

Subsequently, the mechanical properties of the three interpenetrating network hydrogels were evaluated using a universal mechanical testing machine. Compressive moduli were calculated from the stress–strain curves, and the

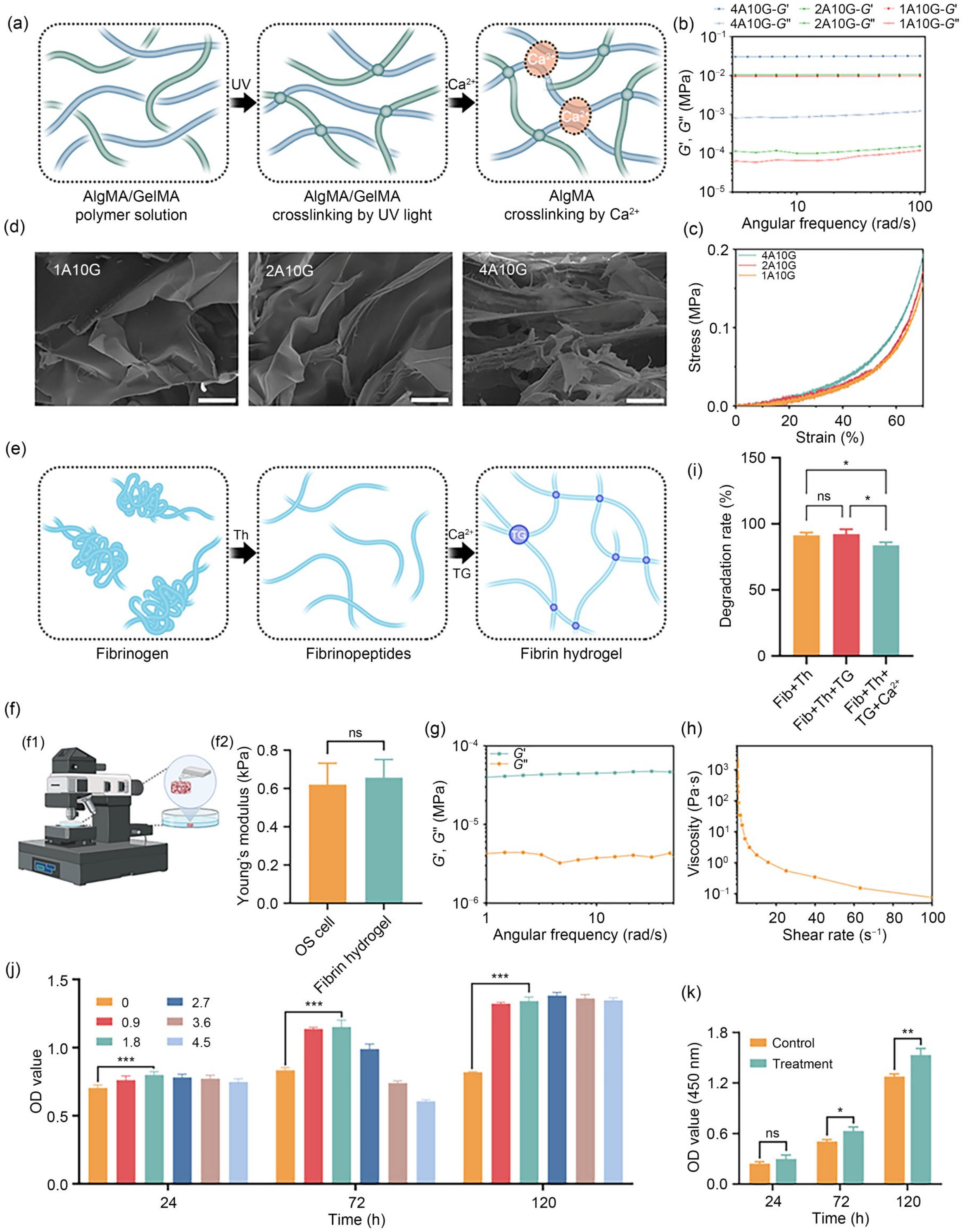

Fig. 2 Design, preparation, and characterization of bioinks. (a) Schematic illustration of the AlgMA/GelMA hydrogel crosslinking mechanism. (b) Storage modulus (G') and loss modulus (G'') of AlgMA hydrogels at different concentrations. (c) Stress–strain curves of AlgMA hydrogels at different concentrations. (d) SEM morphology and porosity of AlgMA hydrogels at different concentrations (scale bar: 100 μm). (e) Schematic illustration of the fibrin hydrogel crosslinking mechanism. (f) Schematic representation of Young's modulus characterization of fibrin hydrogels using AFM (f1) and Young's modulus of osteosarcoma cells and fibrin hydrogels (f2). (g) Storage and loss moduli of the fibrin hydrogels. (h) Rheological properties of the fibrin hydrogels. (i) Degradation rates of three fibrin hydrogels. (j) Evaluation of osteosarcoma cell proliferation at different calcium ion concentrations (0, 0.9, 1.8, 2.7, 3.6, and 4.5 mmol/L) via CCK-8 assay. (k) Evaluation of osteosarcoma tumor spheroid proliferation after calcium ion treatment via CCK-8 assay. Data are expressed as mean±standard deviation (n=3; $^{*}P<0.05$, $^{**}P<0.01$, $^{***}P<0.001$; ns: not significant). 1A10G: 1% AlgMA with 10% GelMA; 2A10G: 2% AlgMA with 10% GelMA; 4A10G: 4% AlgMA with 10% GelMA; Fib: fibrinogen; OD: optical density

compressive moduli of the three interpenetrating network hydrogels were positively correlated with the AlgMA concentration. The compressive moduli of the 1%, 2%, and 4% AlgMA–10% GelMA hydrogels were 42.16, 52.28, and 72.13 kPa, respectively (Fig. 2c). When the AlgMA concentration was 2%, the elastic modulus of the interpenetrating network hydrogel was 52.28 kPa, which is close to the macroscopic collagenous bone tissue biomechanical signal of 55 kPa [32]. The microstructures of the freeze-dried interpenetrating network hydrogels were analyzed using SEM. The hydrogels with interpenetrating networks exhibited a loose porous microstructure, with the pore size becoming denser as the AlgMA concentration increased (Fig. 2d).

Fibrinogen molecules consist of α, β, and γ chains that are crosslinked by two sets of disulfide bonds. Each molecule comprises two external D domains, which are linked to a central E domain through coiled-coil segments. Th cleaves fibrinopeptide A from the fibrinogen α chain, triggering fibrin polymerization and creating a 3D structure that is conducive to cell proliferation (Fig. 2e) [33]. To construct a microenvironment that mimicked the softness of osteosarcoma cells, we first used AFM to measure the Young's modulus of osteosarcoma cells, which was determined to be 620 Pa. Subsequently, fibrin hydrogels were prepared according to the manufacturer's instructions using 10 mg/mL fibrinogen, 10 U/mL Th, and 3% TG. The Young's modulus of the fibrin hydrogels, as measured by AFM, was 657 Pa. No statistically significant difference was observed between the Young's modulus of osteosarcoma cells and that of the fibrin hydrogels ($P>0.05$), indicating the successful construction of a microenvironment that mimics the soft biomechanical signals (Fig. 2f). Rheological analysis revealed that G' of the fibrin hydrogels exceeded G'', exhibiting the characteristics of a solid-like material. This indicated its high elasticity and stability, which provides essential 3D structural support for osteosarcoma tumor spheroids (Fig. 2g).

To further evaluate the printability of the fibrin hydrogels, rheological tests were conducted over a shear rate range of 0.01–100 s^{-1}. The results showed that the fibrin hydrogels exhibited shear-thinning behavior, indicating good rheological properties during the bioprinting process (Fig. 2h). TG was added to the material system to further stabilize the fibrin hydrogels. TG catalyzes the covalent crosslinking of proteins, leading to the formation of γ-glutamyl-ε-lysine side chain peptides, thus stabilizing the fibrin hydrogels [34]. The fibrin hydrogels were degraded using 10 U/mL lumbrokinase. The results showed that the degradation rate of the hydrogels that contained only fibrinogen and Th was 91.36%, whereas those containing fibrinogen, Th, and TG had a degradation rate of 92.25%. Meanwhile, the degradation rate of the fibrin hydrogels that contained fibrinogen, Th, TG, and calcium ions was only 83.86% (Fig. 2i). Therefore, the degradation rate of the fibrin hydrogels containing calcium ions was lower than those of the fibrinogen–Th and fibrinogen–Th–TG hydrogel types ($^{*}P<0.05$).

Concerning the degradation of fibrin hydrogels, we observed no statistical difference in the degradation rates between the fibrin hydrogels generated using fibrinogen and Th alone compared to those generated with the addition of TG or with the further addition of calcium ions. This suggests that TG per se has limited influence on the stability of fibrin hydrogels in the absence of calcium ions. In addition, we found that when fibrinogen, Th, TG, and calcium ions were combined, the resulting fibrin hydrogels exhibited a lower degradation rate, which indicates that calcium ions play a crucial role in enhancing the stability of fibrin hydrogels.

Calcium ions, as important divalent cations, play multiple crucial roles in the system constructed in this study. First, calcium ions undergo ion exchange reactions with the carboxyl groups of the material, promoting the formation of a gel structure. This ion exchange assists in the construction of stable 3D networks and imparts good structural integrity to the material. In particular, ion exchange reactions between calcium ions and the carboxyl groups on AlgMA contribute to the formation of reversible networks, and physical crosslinking enhances the elasticity and durability of the hydrogels. Second, the addition of calcium ions activates TG, facilitating the construction of stable fibrin hydrogels. Calcium ions serve as secondary messengers within cells and are crucial regulatory factors in multiple physiological and biochemical processes, including cell proliferation, apoptosis, and differentiation. During the literature review, we observed that calcium overload therapy has been widely emphasized in the field of oncology. In 2021, Li et al. [35] and Bao et al. [36] proposed calcium overload design strategies aimed at synergistic anti-tumor therapy. Given the role of calcium ions as a critical secondary messenger for cells and the findings of Lim et al. [37], who demonstrated that the addition of calcium ions to chitosan TiO_2 nanotube scaffolds significantly enhanced their biocompatibility, we hypothesized that different concentrations of calcium ions may produce significant differences in the biological effects on osteosarcoma cells. Therefore, we explored various calcium ion concentrations in the present study to further reveal their potential effects. The CCK-8 assay was employed to determine the biological effects of different concentrations of calcium ions on osteosarcoma cells. The results showed that a stable concentration of 1.8 mmol/L calcium ions significantly promoted osteosarcoma cell proliferation (Fig. 2j). Osteosarcoma cells were cultured without (control) and with calcium ions at a concentration of 1.8 mmol/L (treatment) for 2 d to further evaluate the biological effects of calcium ions, and RT-qPCR was used to detect the expression of genes related to the proliferation, migration, and stemness of osteosarcoma cells. Quantitative analysis showed that in the treatment group, the expression level of the proliferation marker Ki-67 (*MKI67*) was significantly upregulated by 1.35-fold compared to that in the control group ($^{***}P<0.001$), whereas the expression levels of the anti-apoptotic gene B-cell lymphoma-2 (*BCL2*) and pro-apoptotic gene Bcl-2 agonist of cell death (*BAD*) increased by 1.85-fold ($^{**}P<0.01$) and 1.3-fold ($P=0.0774$), respectively, compared to those in the control group. Furthermore, the relative expression levels of *BCL2*/*BAD* were normalized between the control and treatment groups, and *BCL2*/*BAD* expression in the treatment group was 1.42-fold higher than that in the control group ($^{**}P<0.01$) (Figs. S1a–S1d in the supplementary information). In addition, expression levels of the migration-related genes vimentin (*VIM*) and cadherin-2 (*CDH2*) were 1.28-fold ($^{**}P<0.01$) and 1.39-fold ($^{***}P<0.001$) higher, respectively, in the treatment group than those in the control group (Figs. S1e and S1f in the supplementary information). Moreover, expression levels of the stemness-related genes *CD133* and *SOX2* were 1.33-fold ($P=0.1428$) and 1.22-fold ($^{*}P<0.05$) higher, respectively, in the treatment group than those in the control group (Figs. S1g and S1h in the supplementary information). Based on these results, we concluded that significant changes occurred in the biological characteristics of osteosarcoma cells in the calcium ion treatment group. In the treatment group, the expression level of *MKI67* was significantly upregulated and those of *BCL2* and *BAD* were also increased markedly. Furthermore, the expression levels of *VIM*, *CDH2*, *CD133*, and *SOX2* were significantly upregulated in the treatment group. These findings suggest that calcium ions can promote the proliferation and migration of osteosarcoma cells, inhibit tumor cell apoptosis, and regulate tumor stemness by affecting the expression of stemness-related genes. In addition, the results of the investigation into the effect of calcium ions on the proliferation of osteosarcoma tumor spheroids demonstrated that calcium ions can stably promote the long-term proliferation of osteosarcoma tumor spheroids (Fig. 2k).

3.2 Construction and characterization of the integrated gradient biomechanical signal-tailored osteosarcoma model (IGBSTOM)

3.2.1 Pre-culture of osteosarcoma tumor spheroids

Three-dimensional tumor spheroids have attracted increasing attention from researchers due to their close resemblance to solid tumors regarding the gradient distribution of oxygen, nutrients, and metabolic byproducts. To construct osteosarcoma 3D tumor spheroids with these properties, we adopted a uniform and highly reproducible ultra-low attachment method for the pre-culture of osteosarcoma tumor spheroids (Fig. 3a), and their successful construction was confirmed by LSCM (Fig. S2a in the supplementary information). According to previous reports, when the diameter of the tumor spheroids reaches approximately 400–600 µm, hypoxia occurs due to oxygen and adenosine triphosphate (ATP) deficiency, resulting in the pathological physiological characteristics of solid tumors [38, 39]. Therefore, we preliminarily optimized the cell densities of the osteosarcoma cells to SD-1, SD-2, and SD-3 for the subsequent pre-culture experiments on osteosarcoma tumor spheroids (Fig. 3b). With increasing culture time, fluorescence microscopy observations at different time points showed that the area of the osteosarcoma tumor spheroids decreased gradually, edges became smoother, and spheroids became more compact. Subsequently, we used ImageJ software to quantitatively analyze the circularity and area of the osteosarcoma tumor spheroids at different time points and cell densities. The results showed that at a cell density of SD-2, the circularities of the osteosarcoma tumor spheroids cultured for 12, 24, and 36 h were 0.80, 0.87, and 0.87 (where 1 indicates a perfect circle, and 0 indicates a straight line), respectively. We found that the circularity did not increase significantly with increasing culture time when the osteosarcoma tumor spheroids were cultured for more than 24 h (Fig. S2b in the supplementary information). Therefore, in the subsequent experiments, we cultured the osteosarcoma tumor spheroids for 24 h. Furthermore, with prolonged culture time, the area of the osteosarcoma tumor spheroids decreased and they became more compact (Fig. S2c in the supplementary information). After pre-culturing the osteosarcoma tumor spheroids for 24 h at a cell density of SD-2, the diameter of the spheroids was approximately 550 µm, and they displayed the pathological physiological characteristics of solid tumors.

3.2.2 Characterization of the IGBSTOM

Fibrinogen loaded with osteosarcoma tumor spheroids was used as the bioink and embedded in an AlgMA/GelMA bioink bath to construct an IGBSTOM. After freeze-drying the constructed osteosarcoma model, SEM was used to characterize the microstructure of the IGBSTOM. SEM revealed a gradient of dense and loose gel pore microstructures (Fig. 3c) and confirmed the successful incorporation of the osteosarcoma tumor spheroids into the gradient biomechanical signal-tailored hydrogel (Fig. 3d). Furthermore, elemental analysis of the common cellular elements via EDS revealed the successful construction of the IGBSTOM (Fig. 3e).

When developing the model for this study, we focused on simulating the mechanics of osteosarcoma and successfully

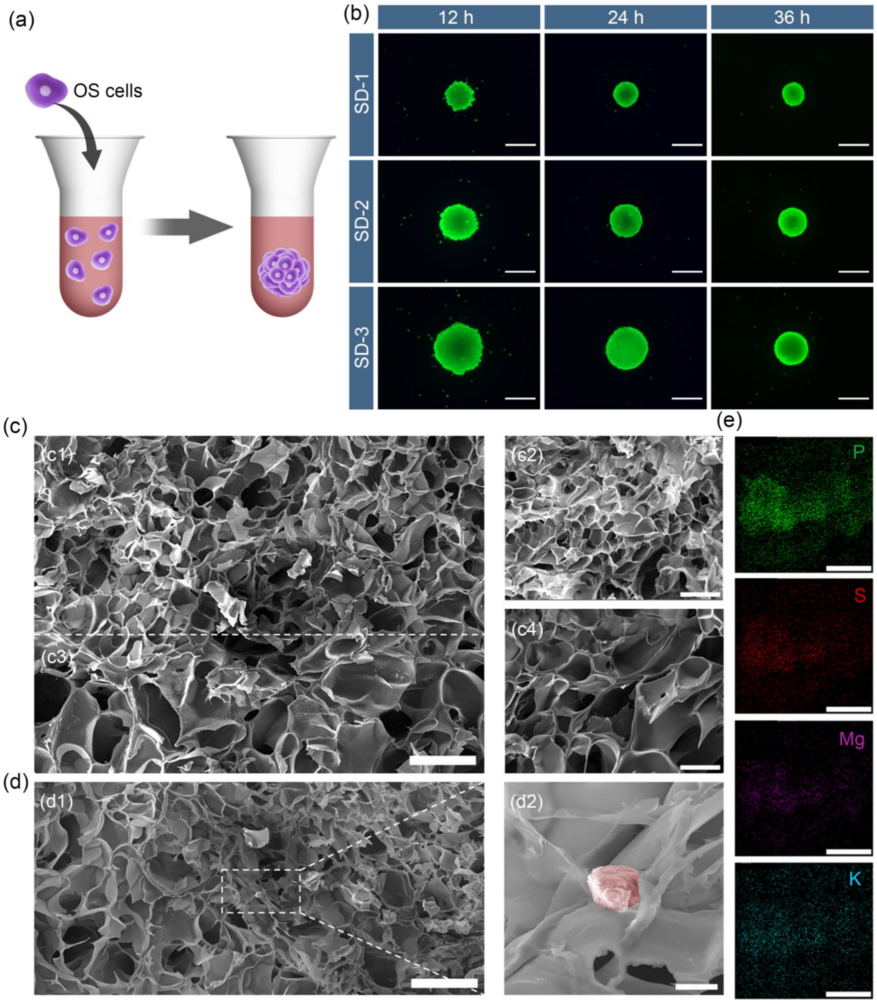

Fig. 3 Characterization of the integrated gradient biomechanical signal-tailored osteosarcoma model. (a) Schematic representation of the osteosarcoma tumor spheroid culture. (b) Morphological characterization of the osteosarcoma tumor spheroids under fluorescence microscopy (scale bar: 500 μm). (c) SEM characterization of the integrated gradient biomechanical signal-tailored osteosarcoma model ((c1, c3) scale bar: 200 μm; (c2, c4) scale bar: 100 μm). (d) An osteosarcoma tumor spheroid in the gradient model (d1, scale bar: 200 μm) and pseudo-staining of the osteosarcoma tumor spheroid (d2, scale bar: 20 μm). (e) EDS analysis of the osteosarcoma tumor spheroid (scale bar: 15 μm)

created a model capable of reproducing its mechanical properties. Compared to the models used currently, our model represents a significant technological advancement in the simulation of the mechanical behavior of osteosarcoma. However, it is important to clarify that despite the success of our model regarding mechanical structure simulation, it does not fully capture the chemical structure of osteosarcoma. The chemical structure plays a crucial role in the complexity of osteosarcoma, influencing its unique properties, such as reactivity, stability, and interactions with other substances. Although our model has made considerable progress in mechanistic simulation, it still has limitations in representing the chemical structure of osteosarcoma. We fully acknowledge this constraint and aim to address it in future studies. Enhancing our ability to simulate the chemical structure of osteosarcoma will enable us to gain a deeper understanding of its biological properties.

3.3 Evaluation of the biocompatibility of the IGBSTOM

Next, we characterized the biocompatibility of the osteosarcoma model using live/dead staining and EdU proliferation assays. We observed that on Days 1 and 7, the Ca^{2+}-OS, Ca^{2+}-S/OS, and Ca^{2+}-G/OS groups showed significantly fewer dead cells than the OS group (Fig. 4a; Fig. S3a in the supplementary information). Quantitative analysis using ImageJ software revealed that on Day 1, the cell viability values in the OS, Ca^{2+}-OS, Ca^{2+}-S/OS, and Ca^{2+}-G/OS groups were 79.93%, 91.19%, 89.97%, and 83.09%, respectively (Fig. S3b in the supplementary information). The cell viability of the Ca^{2+}-OS group was significantly higher than that of the OS group ($^{**}P<0.01$), whereas the cell viability of the Ca^{2+}-G/OS group was only slightly higher than that of the OS group ($P>0.05$). On Day 7, the cell viabilities in the OS, Ca^{2+}-OS, Ca^{2+}-S/OS, and Ca^{2+}-G/OS groups were 81.69%, 90.07%, 84.68%, and 85.04%, respectively (Fig. S3c in the supplementary information). The cell viabilities in the Ca^{2+}-OS and Ca^{2+}-G/OS groups were both significantly higher than that of the OS group ($^{**}P<0.01$ for both). These results indicated that calcium ions can significantly reduce cell apoptosis in an osteosarcoma model, thereby enhancing the cell vitality and showing a trend of relative resistance to osteosarcoma cell apoptosis.

Next, we performed EdU staining to assess cell proliferation in the osteosarcoma model. In EdU staining, cells undergoing DNA synthesis fluoresce as bright green, allowing the assessment of cell proliferation in the model. The proliferation of osteosarcoma cells in the Ca^{2+}-OS, Ca^{2+}-S/OS, and Ca^{2+}-G/OS groups was higher than that in the OS group (Fig. 4b). In particular, in the Ca^{2+}-OS group, a significantly higher proportion of proliferating cells were observed than in the other groups, indicating a significant role of calcium ions in promoting cell proliferation. Although the proliferation level of the Ca^{2+}-G/OS group was slightly lower than that of the Ca^{2+}-OS group, it was still significantly higher than that of the control group. In summary, our results demonstrated good biocompatibility of all osteosarcoma models in terms of live/dead and EdU staining. It is particularly noteworthy that the IGBSTOM exhibited high cell viability and proliferation capabilities, demonstrating excellent biocompatibility.

3.4 Biological effect assessment of the IGBSTOM

Preservation of the natural biological characteristics of tumor cells in in vitro models is considered a crucial factor in tumor research. Tumors possess biological characteristics such as unlimited proliferation, uncontrolled growth, self-renewal, angiogenesis, resistance to apoptosis, invasion and metastasis, genetic variability, and immune evasion [40, 41]. The maintenance of tumor cell stemness is the basis for a deeper understanding of the pathogenesis of tumors and a key factor in the development of new treatment strategies. Therefore, we evaluated the expression of genes and proteins related to tumor stemness, migration, and invasion in an

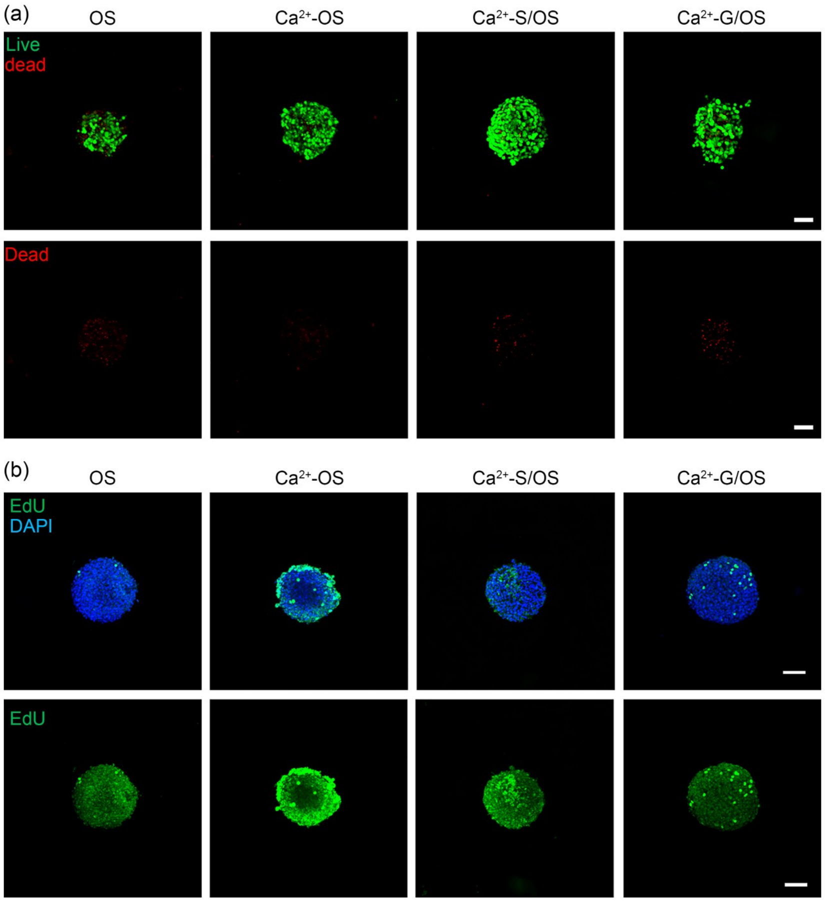

Fig. 4 Characterization of the biocompatibility of the osteosarcoma model. (a) Live/dead staining of the osteosarcoma model on Day 1. Green indicates live cells; red indicates dead cells (scale bar: 100 μm). (b) Evaluation of proliferation in the osteosarcoma model via EdU staining (scale bar: 100 μm)

osteosarcoma model using RT-qPCR and immunofluorescence techniques. First, we assessed the expression of mRNA for the tumor stemness-related marker genes (*CD133* and *SOX2*) and tumor migration and invasion-related marker genes (*VIM* and *CDH2*) using RT-qPCR. This analysis showed that in the Ca^{2+}-G/OS group, the *CD133* and *SOX2* expression levels were 4.72-fold ($^{***}P<$ 0.001) and 2.1-fold ($^{***}P<0.001$) higher, respectively, than those in the OS group (Figs. 5a and 5b). The expression levels of the migration and invasion-related genes, *Snail2*, *VIM*, and *CDH2*, were 1.6-fold ($^{***}P<0.001$), 1.93-fold ($^{***}P<0.001$), and 2.6-fold ($^{***}P<0.001$) higher, respectively, in the Ca^{2+}-G/OS group compared to those in the OS (control) group (Fig. S4b in the supplementary information; Figs. 5c and 5d), whereas the difference in cadherin 1 (*CDH1*) expression was not statistically significant ($P>0.05$; Fig. S4a in the supplementary information). These findings suggested that the IGBSTOM exhibits good stemness characteristics and stronger migration and invasion abilities. In addition, we examined mRNA expression levels of *MKI67*, *BCL2*, and *BAD*. RT-qPCR analysis showed that in the Ca^{2+}-G/OS group, the *MKI67* expression was 1.64-fold ($^{***}P<0.001$) higher, the *BCL2* expression was 1.58-fold ($^{***}P<0.001$) higher, and the *BAD* expression was 0.55-fold ($^{*}P<0.05$) lower than those in the OS group. Normalization of *BCL2*/*BAD* in the Ca^{2+}-G/OS group was 2.89-fold ($^{***}P<0.001$) higher than that in the OS group (Figs. S4c–S4f in the supplementary information). These results suggested that the IGBSTOM exhibits enhanced proliferation promotion and apoptosis inhibition capabilities.

Subsequently, we characterized the expression of tumor stemness, migration, and invasion-related target proteins in all osteosarcoma models using immunofluorescence techniques. Immunofluorescence results showed that the CD133, SOX2, and VIM levels in the Ca^{2+}-G/OS group were significantly higher than those in the other three groups (Figs. 5e and 5f; Figs. S5a–S5d in the supplementary information), which was consistent with the gene expression of *CD133*, *SOX2*, and *VIM*. Taken together, these results demonstrated that the IGBSTOM exhibits higher tumor stemness characteristics and migration and invasion capabilities while maintaining the biological characteristics of natural tumors.

3.5 Establishment of the subcutaneous osteosarcoma model in vivo

To assess the tumorigenic potential of the tumor models and preserve the innate biological characteristics of the implanted tumor cells, all osteosarcoma models were implanted subcutaneously into BALB/c nude mice. Prior to implantation, we pre-cultured the four tumor models for 4 d to allow the cells to fully adapt to the new growth environment. Fourteen days after implantation, we euthanized all animals, harvested the tumor tissues, and performed H&E and immunofluorescence staining (Fig. 6a). Tumors were successfully formed in all tumor models after implantation (Fig. 6b). The Ca^{2+}-OS group had the largest tumor volume, possibly due to the proliferative effect of calcium ions on osteosarcoma cells, and the Ca^{2+}-S/OS group had the smallest tumor volume, which may be due to its weak proliferative capacity. This finding is in line with the proliferative capacity of ECM, which has been reported to be soft [42].

H&E staining revealed that the osteosarcoma cells in all tumor models exhibited irregular morphology and deeply stained nuclei. In addition, in the Ca^{2+}-S/OS and Ca^{2+}-G/OS groups, we observed residual bioink that exhibited weak staining. Interestingly, in the Ca^{2+}-G/OS group, we observed the presence of nest-like structures consisting of aggregated tumor cells (Fig. 6c). It is well-known that in natural solid tumors, cancer cells tend to aggregate into clusters or nests, forming structures commonly referred to as “cancer nests.” These nest-like structures provide an organized tissue architecture that is conducive to close cellular arrangement and interactions, thereby promoting cell proliferation and infiltration and facilitating tumor growth and metastasis. The presence of nest-like structures is often associated with treatment resistance and tumor malignancy and prognosis. Larger and more complex nest structures typically indicate higher invasive and metastatic potential and a poorer prognosis [43]. In vitro tumor models that reproduce cancer nest-like structures are, therefore, of great significance for their ability to simulate the physiopathological characteristics of natural solid tumors, allowing for in-depth exploration of the pathogenesis of cancer and evaluation of the treatment effectiveness.

We conducted immunofluorescence staining for tumor proliferation marker Ki67, tumor stemness markers CD133 and SOX2, and vascular markers CD31 and α-SMA. In the Ca^{2+}-G/OS model, we observed high expression of CD133 and Ki67 (Fig. 6d). Furthermore, SOX2 was expressed in all models but was significantly higher in the Ca^{2+}-G/OS osteosarcoma model than in other groups (Fig. 6e). Expression of the vascular markers CD31 and α-SMA indicated that all four tumor models underwent vascularization, with larger vessel diameters observed in the OS group compared to those in the Ca^{2+}-S/OS and Ca^{2+}-G/OS groups, which could be possibly attributed to the restricted vessel growth by the hydrogel (Fig. 6f).

Based on these results, we conclude that the osteosarcoma model tailored with integrated gradient biomechanical signaling exhibits enhanced tumor stemness and proliferative activity and successfully reproduces the cancer nest-like

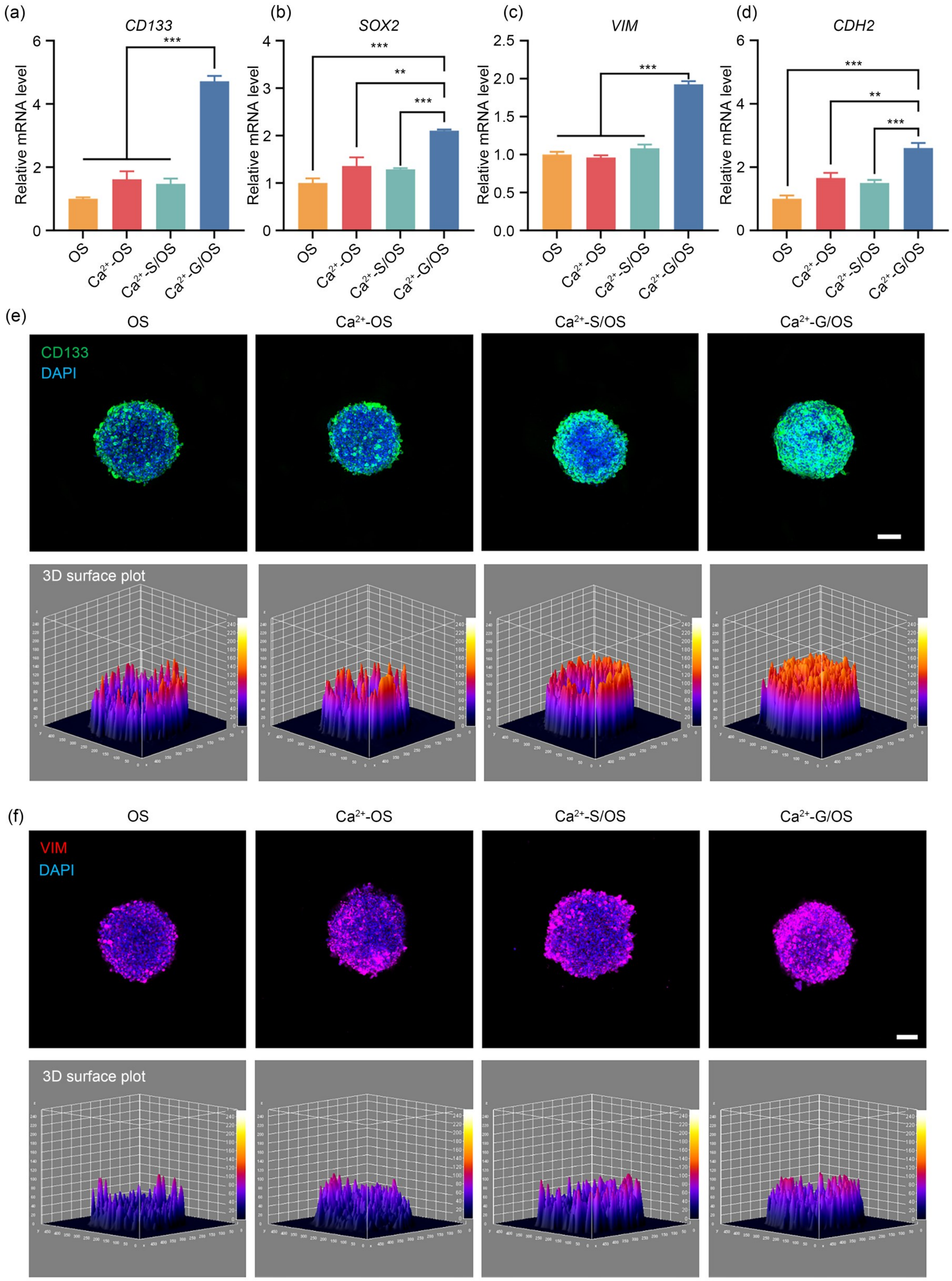

Fig. 5 Expression of tumor stemness and migration-related markers. mRNA expression levels of *CD133* (a), *SOX2* (b), *VIM* (c), and *CDH2* (d). Data are expressed as mean±standard deviation (n=3; $^{**}P<0.01$, $^{***}P<0.001$). Immunofluorescence images showing the expression of CD133 (e) and the migration marker VIM (f). Scale bar: 100 μm

structures commonly found in tumor tissues. This discovery provides a solid experimental foundation for the further exploration of tumor biology and the development of more effective treatment strategies.

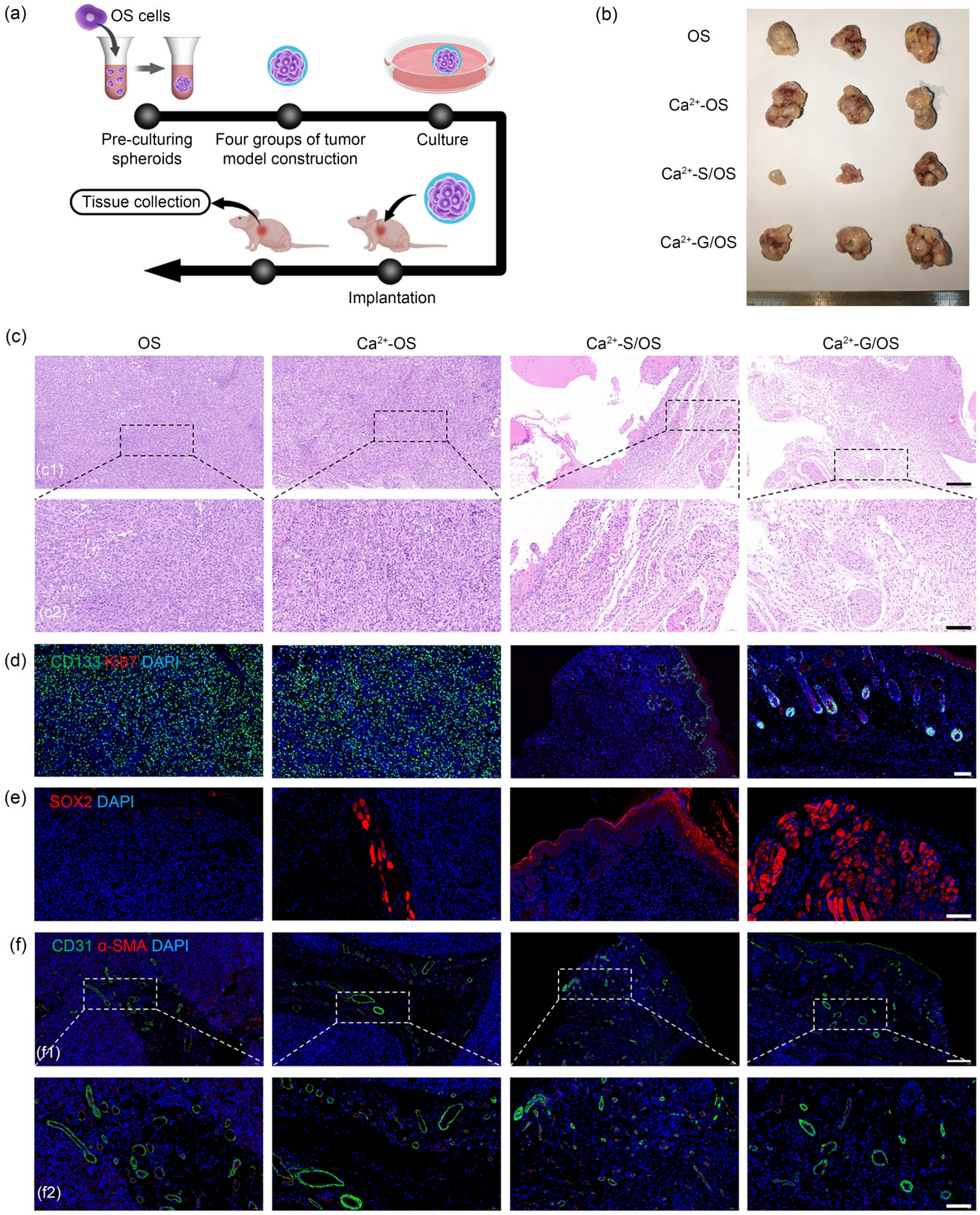

Fig. 6 In vivo subcutaneous assessment of osteosarcoma model establishment. (a) Schematic illustration of the entire process of animal testing. (b) Macroscopic view of the large tumors after collection. (c) H&E staining of the osteosarcoma models in each group (c1, scale bar: 100 µm; c2, scale bar: 50 µm). (d, e) Immunofluorescence images of tumor proliferation marker (Ki67) and stemness markers (CD133 and SOX2); scale bar: 50 µm. (f) Immunofluorescence images of vascular markers (CD31 and α-SMA) in the osteosarcoma models of each group (f1, scale bar: 100 µm; f2, scale bar: 50 µm)

3.6 Drug sensitivity and RNA sequencing analysis of the IGBSTOM

In vitro tumor models play a crucial role in drug development for basic research and clinical practice, demonstrating vast prospects and tremendous potential. These models faithfully mimic the complex biological characteristics of tumors and provide efficient and cost-effective platforms for drug screening, thus offering crucial support for drug development and clinical translation research. Therefore, we conducted drug sensitivity tests on our tumor models. First, we assessed the drug penetration of 3D tumor models using rhodamine B. The molecular weight of rhodamine B (479.01 g/mol) is similar to that of commonly used chemotherapeutic drugs, making it suitable for chemotherapy drug simulations. The results of the drug sensitivity tests showed that rhodamine B penetrated the entire 3D osteosarcoma model within 2 h, confirming good drug penetration of the 3D model (Fig. S6a in the supplementary information). Subsequently, we performed drug sensitivity experiments using the tumor models. We selected the first-line chemotherapy drugs, doxorubicin and methotrexate, for drug sensitivity testing. Doxorubicin is an anthracycline anticancer chemotherapeutic drug that inhibits cancer cell growth and division by preventing DNA replication and inducing apoptosis [44]. Methotrexate is an antimetabolite drug that inhibits dihydrofolate reductase in cells, thereby reducing the levels of intracellular dihydrofolate, affecting the synthesis of DNA and RNA, and hindering cancer cell growth and division [45, 46]. The above-mentioned in vitro osteosarcoma models were co-incubated with various concentrations of methotrexate and doxorubicin (0, 0.1, 1, 10, 100, and 500 μmol/L), and cell viabilities were evaluated after 48 h. The IC_{50} values of doxorubicin and methotrexate for the Ca^{2+}-G/OS group were 198 and 202.3 μmol/L, respectively, whereas for the OS group, the values were 22.09 and 57.16 μmol/L, respectively. Therefore, the Ca^{2+}-G/OS group exhibited higher drug resistance compared to the control group (Figs. 7a and 7b). This phenomenon may be related to the enhanced stemness of cells in the Ca^{2+}-G/OS group, which increases their drug resistance.

To further validate the feasibility of the IGBSTOM and explore its potential mechanisms, we conducted transcriptome sequencing analysis. We aimed to comprehensively analyze the gene expression profiles in the tumor models and investigate the potential signaling pathways and regulatory networks involved. Through this in-depth transcriptomic study, we hoped to reveal the molecular mechanisms underlying the formation of a tumor model, thereby providing an important theoretical and experimental basis for further biological research and clinical treatment. Transcriptome analysis was performed for the Ca^{2+}-G/OS and OS groups

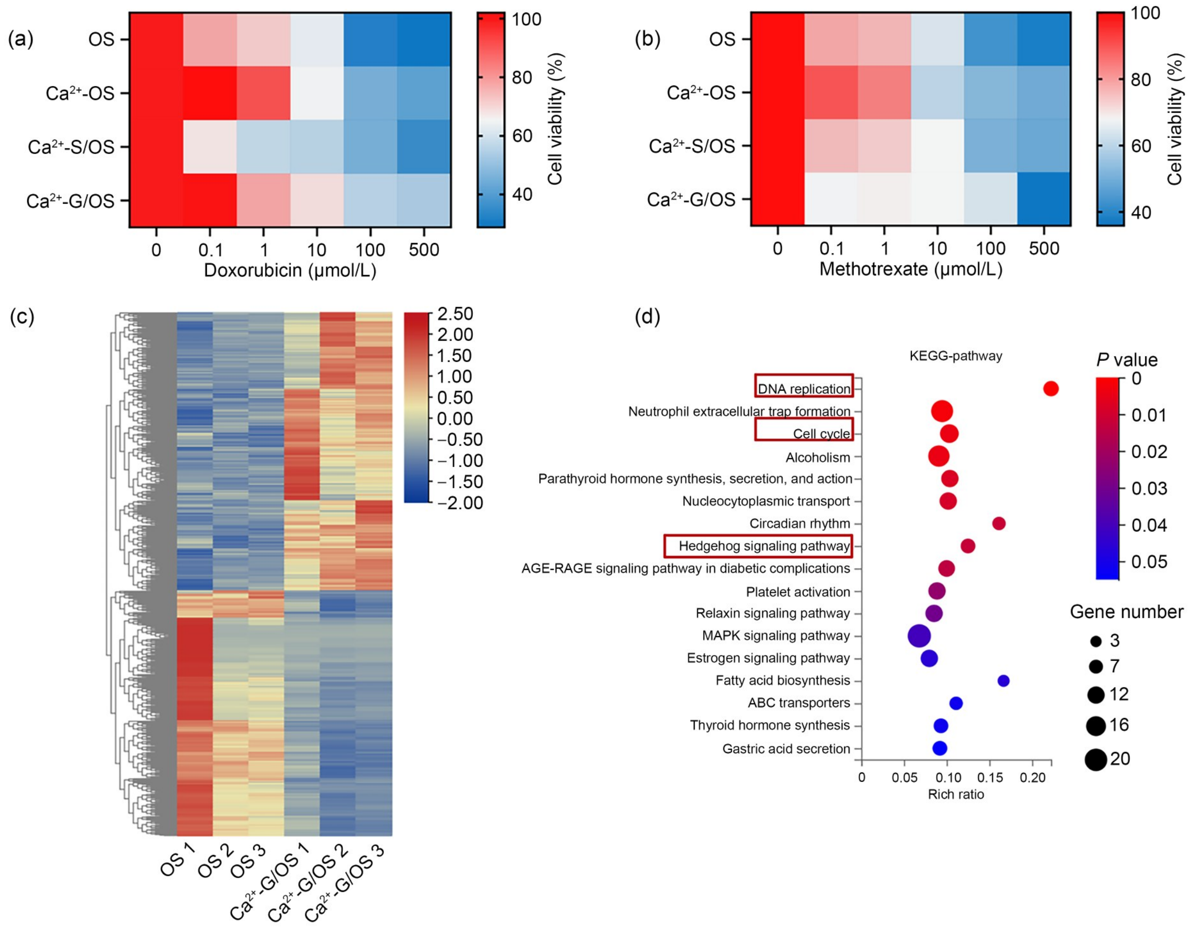

Fig. 7 Drug sensitivity and transcriptome analysis of the in vitro osteosarcoma model. Sensitivity of the models to doxorubicin (a) and methotrexate (b). (c) Heatmap of DEG clustering. (d) KEGG pathway enrichment analysis of DEGs. Pathways of interest are highlighted in red boxes

using RNA sequencing technology to study the molecular changes in depth; the analysis revealed 380 upregulated and 339 downregulated genes (Fig. S6b in the supplementary information). These results indicated significant gene expression changes between the two groups, laying the foundation for further exploration of the molecular mechanisms of osteosarcoma models.

To deeply explore the patterns of DEGs, we performed systematic cluster analysis (Fig. 7c). This analysis aimed to reveal patterns of gene expression and cluster affiliation, thereby enhancing our understanding of the regulatory network of DEGs. To further elucidate the functions and potential pathways of these DEGs, we performed KEGG pathway enrichment analysis. By examining the top 17 significantly enriched pathways, we gained insights into the functions of DEGs. The results of the enrichment analysis suggested that these DEGs may be involved in key biological processes, such as DNA replication, cell cycle, and hedgehog (HH) signaling pathway (Fig. 7d). This suggests that the microenvironmental osteosarcoma model with integrated gradient mechanics may potentially impact these signaling pathways. In particular, the regulatory mechanisms of DNA replication and cell cycle are central to various tumor-associated signaling pathways. In addition, the enrichment of the HH signaling pathway suggests that this pathway may play a key role in osteosarcoma genesis, development, and signature expression.

In the present study, the Ca^{2+}-G/OS group showed enhanced resistance to chemotherapeutic agents compared with the OS group. In line with recent findings on the supportive role of the biomechanical environment for cancer stem cells, niche stiffness maintains cancer stemness through the phase separation of transcriptional coactivator with PDZ-binding motif (TAZ) and homeobox protein NANOG (NANOG) [47]. Therefore, we hypothesized that osteosarcomas in the Ca^{2+}-G/OS group may enrich tumor stem cells, thereby enhancing their resistance to chemotherapeutic agents. To fully explore the impact of mechanical signaling on cellular phenotype and function, we conducted an in-depth analysis of the transcriptome data and GSEA. As shown in Fig. S6c (supplementary information), although the mitogen-activated protein kinase signaling pathway was more likely to be identified as a potential therapeutic target, it does not indicate that mechanical signaling does not play a role. When GSEA software assesses gene set enrichment, gene trends are considered. When some genes are upregulated while others are downregulated, this may result in an attenuated enrichment signal for that gene set in GSEA. Therefore, GSEA may have failed to show a significant enrichment effect. However, this analysis still provides valuable insights and guides the direction of future studies.

In previous sections, we have detailed our research methods and results. To fully assess the validity of our model, we will now compare and discuss our findings with the 3D models currently widely used. First, our model has made significant technological advances in simulation of the mechanics of osteosarcoma. Compared to traditional 2D tumor models and the 3D scaffold model for osteosarcoma tissue engineering developed by Molina et al. [48], our model more accurately reproduces the high cell density of osteosarcoma-like tissues and exhibits greater flexibility and precision in addressing the complex mechanical properties of osteosarcoma. This enables us to gain a deeper understanding of the behavior of osteosarcoma in both physiological and pathological states. Second, when comparing the ability of our model to simulate the biological properties of osteosarcoma with that of existing 3D models, we found that our model showed advantages in several aspects. For example, when implanted in nude mice, our model reproduced the cancer nest-like structure of natural tumors and could simulate the interactions of osteosarcoma cells with the microenvironment more accurately than the current models. This precise simulation ability allows the examination of the complex biological mechanisms of osteosarcoma and provides new ideas for developing more effective therapeutic approaches. Although our model demonstrates unique value in some aspects, it has limitations compared to the advanced 3D models developed by Meng et al. [49]. Their programmable release capsule, which accurately constructs tumor structures and enables precise spatiotemporal control of signaling molecular gradients, dynamically regulates cellular behaviors at a local level. In contrast, our model still has limitations in key areas such as chemical structure simulation. Addressing these limitations will be the focus of our future research and improvement efforts. We expect that with continuous technological advances and deeper research, we will be able to develop even better models for the improved understanding and treatment of osteosarcoma.

4 Conclusions

To the best of our knowledge, this is the first study to successfully construct a gradient biomechanical signal-tailored osteosarcoma model that reproduces the pathophysiological features of a natural osteosarcoma. Using advanced bioprinting equipment, we carefully designed and optimized a bioink to construct a highly integrated biomechanical signal-tailored osteosarcoma model. Notably, the bioprinted osteosarcoma model accurately mimicked the gradient biomechanical signal properties of osteosarcoma and exhibited its more significant tumor stemness, proliferation, and migration. Importantly, the model successfully reproduced the pathophysiological characteristics of cancer nest-like structures found in a natural tumor model, providing strong support for our in-depth understanding of the pathogenesis of osteosarcoma. Transcriptome analysis revealed the potential regulatory pathways of gradient biomechanical signaling in the osteosarcoma model, providing valuable clues for subsequent drug screening, therapeutic studies, and exploration of drug resistance and metastasis mechanisms. In summary, this study provides a highly valuable research platform for the in-depth understanding of the pathogenesis of osteosarcoma, drug screening, and therapeutic studies and the exploration of drug resistance and metastasis mechanisms.

Supplementary Information The online version contains supplementary material available at https://doi.org/10.1631/bdm.2400108.

Acknowledgements The authors appreciate financial support from the National Key R&D Program of China (No. 2022YFA1104600), 2022 Lingang Laboratory "Seeking Outstanding Youth Program" Open Project (No. LGQS-202206-04), Shanghai Ninth People's Hospital–Shanghai Jiao Tong University School of Medicine–Shanghai University of Science and Technology Cross-funded Collaborative Program (No. JYJC202233), the National Natural Science Foundation of China (No. 82372377), Biomaterials and Regenerative Medicine Institute Cooperative Research Project by Shanghai Jiao Tong University School of Medicine (No. 2022LHBO8), Shanghai Key Laboratory of Orthopaedic Implants, Department of Orthopaedics by Shanghai Ninth People's Hospital–Shanghai Jiao Tong University School of Medicine (No. KFKT202206), the Key R&D Program of Jiangsu Province Social Development Project (No. BE2022708), and the Project of Shanghai Science and Technology Commission (No. 22015820100). We thank Saoshuai Song and Jianpeng Zhang for their help with this study. We would like to express our gratitude to BioRender for its valuable assistance in creating figures for this manuscript.

Author contributions Conceptualization: XLM, CRZ, and JWW. Formal analysis: XLM, YR, and HBW. Investigation: XLM, HBW, LQ, and WQK. Methodology: HW, XY, YHL, HY, DX, and GXX. Resources: ZJM and JWW. Supervision: CRZ and JWW. Writing: XLM, YR, and HBW.

Declarations

Conflict of interest The authors declare that they have no conflict of interest.

Ethical approval This study was conducted in accordance with the guidelines of the Animal Care and Use Committee (ACUC) of Shanghai Jiao Tong University. The experimental protocol was approved by the ACUC (Approval No. A2024001).

Data availability The data that support the findings of this study are available from the corresponding authors upon reasonable request.

References

1. Biermann JS, Chow W, Reed DR et al (2017) NCCN guidelines insights: bone cancer, version 2.2017. J Natl Compr Canc Netw 15(2):155–167. https://doi.org/10.6004/jnccn.2017.0017
2. Miller BJ, Cram P, Lynch CF et al (2013) Risk factors for metastatic disease at presentation with osteosarcoma: an analysis of the SEER database. J Bone Joint Surg Am 95(13):e89. https://doi.org/10.2106/JBJS.L.01189
3. Birgersdotter A, Sandberg R, Ernberg I et al (2005) Gene expression perturbation in vitro—a growing case for three-dimensional (3D) culture systems. Semin Cancer Biol 15(5): 405–412. https://doi.org/10.1016/j.semcancer.2005.06.009
4. Astashkina A, Mann B, Grainger DW (2012) A critical evaluation of in vitro cell culture models for high-throughput drug screening and toxicity. Pharmacol Ther 134(1):82–106. https://doi.org/10.1016/j.pharmthera.2012.01.001
5. Stowers RS, Shcherbina A, Israeli J et al (2019) Matrix stiffness induces a tumorigenic phenotype in mammary epithelium through changes in chromatin accessibility. Nat Biomed Eng 3(12):1009–1019. https://doi.org/10.1038/s41551-019-0420-5
6. Wisdom KM, Adebowale K, Chang J et al (2018) Matrix mechanical plasticity regulates cancer cell migration through confining microenvironments. Nat Commun 9(1):4144. https://doi.org/10.1038/s41467-018-06641-z
7. Safaei S, Sajed Roya, Shariftabrizi A et al (2023) Tumor matrix stiffness provides fertile soil for cancer stem cells. Cancer Cell Int 23(1):143. https://doi.org/10.1186/s12935-023-02992-w
8. Sun YC, Li H, Chen QF et al (2021) The distribution of liver cancer stem cells correlates with the mechanical heterogeneity of liver cancer tissue. Histochem Cell Biol 156(1):47–58. https://doi.org/10.1007/s00418-021-01979-w
9. Xu WW, Mezencev R, Kim B et al (2012) Cell stiffness is a biomarker of the metastatic potential of ovarian cancer cells. PLoS ONE 7(10):e46609. https://doi.org/10.1371/journal.pone.0046609
10. Plodinec M, Loparic M, Monnier CA et al (2012) The nanomechanical signature of breast cancer. Nat Nanotechnol 7(11):757–765. https://doi.org/10.1038/nnano.2012.167
11. Cates JMM, Schoenecker JG (2016) Proximal location in extremity long bones is a poor prognostic factor for osteosarcoma: a retrospective cohort study of 153 patients. Acta Oncol 8(55): 1036–1039. https://doi.org/10.3109/0284186X.2016.1156740
12. Northcott JM, Dean IS, Mouw JK et al (2018) Feeling stress: the mechanics of cancer progression and aggression. Front Cell Dev Biol 6:17. https://doi.org/10.3389/fcell.2018.00017
13. Chow T, Wutami I, Lucarelli E et al (2021) Creating in vitro three-dimensional tumor models: a guide for the biofabrication of a primary osteosarcoma model. Tissue Eng Part B Rev 27(5): 514–529. https://doi.org/10.1089/ten.TEB.2020.0254
14. Leitner N, Hlavatý J, Ertl R et al (2022) Lipid droplets and perilipins in canine osteosarcoma. Investigations on tumor tissue, 2D and 3D cell culture models. Vet Res Commun 46(4):1175–1193. https://doi.org/10.1007/s11259-022-09975-8
15. Ren JX, Zhao C, Sun RZ et al (2024) Augmented drug resistance of osteosarcoma cells within decalcified bone matrix scaffold: the role of glutamine metabolism. Int J Cancer 154(9): 1626–1638. https://doi.org/10.1002/ijc.34841
16. He JC, Chen CC, Chen L et al (2022) Honeycomb-like hydrogel microspheres for 3D bulk construction of tumor models. Research 2022:9809763. https://doi.org/10.34133/2022/9809763
17. Gungor-Ozkerim PS, Inci I, Zhang YS et al (2018) Bioinks for 3D bioprinting: an overview. Biomater Sci 6(5):915–946. https://doi.org/10.1039/C7BM00765E

18. Mousavi A, Hedayatnia A, van Vliet PP et al (2024) Development of photocrosslinkable bioinks with improved electromechanical properties for 3D bioprinting of cardiac BioRings. Appl Mater Today 36:102035. https://doi.org/10.1016/j.apmt.2023.102035
19. Parak A, Pradeep P, du Toit LC et al (2019) Functionalizing bioinks for 3D bioprinting applications. Drug Discov Today 24(1): 198–205. https://doi.org/10.1016/j.drudis.2018.09.012
20. Cao BJ, Lin JM, Tan J et al (2023) 3D-printed vascularized biofunctional scaffold for bone regeneration. Int J Bioprint 9(3): 702. https://doi.org/10.18063/ijb.702
21. Pereira I, Lopez-Martinez MJ, Villasante A et al (2023) Hyaluronic acid-based bioink improves the differentiation and network formation of neural progenitor cells. Front Bioeng Biotechnol 11:1110547. https://doi.org/10.3389/fbioe.2023.1110547
22. Wang D, Maharjan S, Kuang X et al (2022) Microfluidic bioprinting of tough hydrogel-based vascular conduits for functional blood vessels. Sci Adv 8(43):eabq6900. https://doi.org/10.1126/sciadv.abq6900
23. Chen HY, Ma XX, Zhang MQ et al (2023) Injectable and biofunctionalized fibrin hydrogels co-embedded with stem cells induce hair follicle genesis. Regen Biomater 10:rbac086. https://doi.org/10.1093/rb/rbac086
24. Murphy SV, Atala A (2014) 3D bioprinting of tissues and organs. Nat Biotechnol 32(8):773–785. https://doi.org/10.1038/nbt.2958
25. Datta P, Dey M, Ataie Z et al (2020) 3D bioprinting for reconstituting the cancer microenvironment. npj Precis Oncol 4(1):18. https://doi.org/10.1038/s41698-020-0121-2
26. Daly AC, Prendergast ME, Hughes AJ et al (2021) Bioprinting for the biologist. Cell 184(1):18–32. https://doi.org/10.1016/j.cell.2020.12.002
27. Cui X, Hartanto Y, Zhang H et al (2017) Advances in multicellular spheroids formation. J R Soc Interface 14(127):20160788. https://doi.org/10.1098/rsif.2016.0877
28. Shams E, Barzad MS, Mohamadnia S et al (2022) A review on alginate-based bioinks, combination with other natural biomaterials and characteristics. J Biomater Appl 37(2):355–372. https://doi.org/10.1177/08853282221085690
29. Loessner D, Meinert C, Kaemmerer E et al (2016) Functionalization, preparation and use of cell-laden gelatin methacryloyl-based hydrogels as modular tissue culture platforms. Nat Protoc 11(4):727–746. https://doi.org/10.1038/nprot.2016.037
30. Li LB, Fang YP, Vreeker R et al (2007) Reexamining the egg-box model in calcium−alginate gels with X-ray diffraction. Biomacromolecules 8(2):464–468. https://doi.org/10.1021/bm060550a
31. Arya AD, Hallur PM, Karkisaval AG et al (2016) Gelatin methacrylate hydrogels as biomimetic three-dimensional matrixes for modeling breast cancer invasion and chemoresponse in vitro. ACS Appl Mater Interfaces 8(34):22005–22017. https://doi.org/10.1021/acsami.6b06309
32. Müller DA, Silvan U (2019) On the biomechanical properties of osteosarcoma cells and their environment. Int J Dev Biol 63(1–2):1–8. https://doi.org/10.1387/ijdb.190019us
33. Mosesson MW (2005) Fibrinogen and fibrin structure and functions. J Thromb Haemost 3(8):1894–1904. https://doi.org/10.1111/j.1538-7836.2005.01365.x
34. Lorand L, Conrad SM (1984) Transglutaminases. Mol Cell Biochem 58(1-2):9–35. https://doi.org/10.1007/BF00240602
35. Li YL, Zhou S, Song HZ et al (2021) $CaCO_3$ nanoparticles incorporated with KAE to enable amplified calcium overload cancer therapy. Biomaterials 277:121080. https://doi.org/10.1016/j.biomaterials.2021.121080
36. Bao WE, Liu M, Meng JQ et al (2021) MOFs-based nanoagent enables dual mitochondrial damage in synergistic antitumor therapy via oxidative stress and calcium overload. Nat Commun 12(1):6399. https://doi.org/10.1038/s41467-021-26655-4
37. Lim SS, Chai CY, Loh HS (2017) In vitro evaluation of osteoblast adhesion, proliferation and differentiation on chitosan-TiO_2 nanotubes scaffolds with Ca^{2+} ions. Mater Sci Eng C 76: 144–152. https://doi.org/10.1016/j.msec.2017.03.075
38. Bertuzzi A, Fasano A, Gandolfi A et al (2010) Necrotic core in EMT6/Ro tumour spheroids: is it caused by an ATP deficit? J Theor Biol 262(1):142–150. https://doi.org/10.1016/j.jtbi.2009.09.024
39. Nath S, Devi GR (2016) Three-dimensional culture systems in cancer research: focus on tumor spheroid model. Pharmacol Ther 163:94–108. https://doi.org/10.1016/j.pharmthera.2016.03.013
40. Zhao Y, Dong QZ, Li JH et al (2018) Targeting cancer stem cells and their niche: perspectives for future therapeutic targets and strategies. Semin Cancer Biol 53:139–155. https://doi.org/10.1016/j.semcancer.2018.08.002
41. Reya T, Reya T, Morrison SJ et al (2001) Stem cells, cancer, and cancer stem cells. Nature 414(6859):105–111. https://doi.org/10.1038/35102167
42. Li S, Bai HX, Chen XY et al (2020) Soft substrate promotes osteosarcoma cell self-renewal, differentiation, and drug resistance through miR-29b and its target protein Spin 1. ACS Biomater Sci Eng 6(10):5588–5598. https://doi.org/10.1021/acsbiomaterials.0c00816
43. Arienzo F, Valenti A, Ricci P et al (2024) Metastatic upper tract urothelial carcinoma with nest-like features presenting as malignant pleural effusion. Diagn Cytopathol 52(6):E124–E128. https://doi.org/10.1002/dc.25293
44. Nitiss JL (2009) Targeting DNA topoisomerase II in cancer chemotherapy. Nat Rev Cancer 9(5):338–350. https://doi.org/10.1038/nrc2607
45. Gallego B, Murillo D, Rey V et al (2022) Addressing doxorubicin resistance in bone sarcomas using novel drug-resistant models. Int J Mol Sci 23(12):6425. https://doi.org/10.3390/ijms23126425
46. Meazza C, Asaftei SD (2021) State-of-the-art, approved therapeutics for the pharmacological management of osteosarcoma. Expert Opin Pharmacother 22(15):1995–2006. https://doi.org/10.1080/14656566.2021.1936499
47. Liu X, Ye YY, Zhu LL et al (2023) Niche stiffness sustains cancer stemness via TAZ and NANOG phase separation. Nat Commun 14(1):238. https://doi.org/10.1038/s41467-023-35856-y
48. Molina ER, Chim LK, Salazar MC et al (2019) Mechanically tunable coaxial electrospun models of YAP/TAZ mechanoresponse and IGF-1R activation in osteosarcoma. Acta Biomater 100:38–51. https://doi.org/10.1016/j.actbio.2019.09.029
49. Meng F, Meyer CM, Joung D et al (2019) 3D bioprinted in vitro metastatic models via reconstruction of tumor microenvironments. Adv Mater 31(10):e1806899. https://doi.org/10.1002/adma.201806899